IEEE Open Journal of
Power Electronics

Received 19 December 2024; revised 19 February 2025; accepted 26 February 2025. Date of publication 27 February 2025; date of current version 25 April 2025. The review of this article was arranged by Associate Editor Yongchang Zhang.

Digital Object Identifier 10.1109/OJPEL.2025.3546752

Automatic Tuning of Extended Kalman Filter in Sensorless Synchronous Reluctance Motor Drives

SAVERIO RIGON [1] (Member, IEEE), BENEDIKT HAUS [1], PAOLO MERCORELLI [1] (Member, IEEE), AND MAURO ZIGLIOTTO [2] (Senior Member, IEEE)

[1]Institute for Production Technology and Systems (IPTS), Leuphana University of Lüneburg, 21335 Lüneburg, Germany
[2]Department of Management and Engineering, Università degli Studi di Padova, 36100 Vicenza, Italy

CORRESPONDING AUTHOR: SAVERIO RIGON (e-mail: saverio.rigon@phd.unipd.it)

This work was supported in part by the Ph.D. Scholarship on Innovation Topics under Grant PON 2014-2020 Action IV.4 and in part by the Fondazione Aldo Gini. The publication was funded by the German Research Foundation (DFG).

ABSTRACT A substantial reduction in the human environmental footprint can be achieved through the use of more efficient motors, such as synchronous reluctance motors (SynRM). As low-cost motors, SynRMs are commonly employed in sensorless AC drives. Sensorless algorithms based on the Extended Kalman Filter (EKF) offer several advantages, but they require a time-consuming trial-and-error tuning procedure. This paper proposes the automatic tuning of the EKF through a second Kalman Filter (KF) in a primary–secondary (PS) configuration. The two KFs work concurrently: the first estimates the required quantities for machine control, and the second updates the process noise statistics of the first KF. The second KF is much easier to tune, requiring only one non-critical parameter. Experimental results confirm the validity of this approach.

INDEX TERMS Kalman filter, adaptive kalman filter, sensorless, synchronous reluctance motor (SynRM), AC machines, primary–secondary Kalman Filter.

I. INTRODUCTION

The recent accessibility of affordable and powerful computational resources is rendering synchronous reluctance motors (SynRMs) a feasible substitute for motors reliant on rare earth permanent magnet synchronous motors (PMSMs), which have drawn criticism for their significant environmental footprint. Compared to their major competitor, the induction motor (IM), SynRMs offer greater efficiency and a superior torque-to-volume ratio, positioning them to gradually compete in various applications, including the automotive field.

Achieving reliability and cost reduction in SynRM drives necessitates sensorless control. Deterministic algorithms, such as hybrid flux observers [1], typically rely on a predefined set of equations or rules for estimation. While effective under specific conditions, they do not inherently account for noise characteristics, making them more susceptible to suboptimal state estimation when measurements are noisy or the model is inaccurate. As a valid alternative, Extended Kalman Filter (EKF), widely used for PMSM and IM drives [2], [3], appears to be a suitable candidate for SynRM drives as well, although the pronounced magnetic nonlinearity of the motor presents additional challenges.

Currently, the scientific literature on the application of EKF to SynRM drives remains quite limited. In [4], angle estimation offsets caused by inductance mismatch within a SynRM sensorless control scheme based on active back EMF estimation are alleviated by switching between multiple Kalman filters based on different models with differing parameter sensitivities, in order to robustify the estimation for a wider range of angles. The same group presented this concept in [5], where the estimated EMF is combined with adaptive filtering and integration to obtain a smooth position estimate. These works derive (single, or multiple switched) Kalman filters based on linear steady-state models with the direct goal of estimating the back EMF and use this signal to extract the position information, like it is also done in [6]. While this multi-step and indirect angle estimation procedure is demonstrated to work satisfactorily in practice, the back EMF is selected as

an intermediate stochastic variable, a compromise that ignores parts of the actual physical interdependence/coupling between currents and rotor angle within the KF-models, but allows to keep the models simple and linear, followed by a deterministic (potentially unrobust and/or slow) filtered calculation of the angle based on this back EMF. In contrast to such serialization of multiple different methodologies, each with their own tuning parameters that must be harmonized, the contribution at hand applies the probabilistic viewpoint within a single framework directly to the whole nonlinear SynRM model, directly treating the angle as the variable to be estimated within the Kalman filtering algorithm.

The EKF is based on a Taylor series approximation of the nonlinear model. While this approximation helps in solving the nonlinear problem, the EKF remains susceptible to random noise, and incorrect characterization of this noise can lead to reduced filtering accuracy and potential divergence. Therefore, variance estimation is of primary concern [7], [8], [9]. Over the last few decades, this topic has not been definitively solved and has stimulated active research, as briefly recalled in the following.

A. EKF TUNING TECHNIQUES

Excluding trial-and-error manual tuning, which is still widely proposed but requires experienced engineers, many other tuning solutions were proposed over the years. A particularly imaginative one that was proposed in the 1970s [10] builds statistics based on the noise sample generated by the filter itself, obtained as the difference between estimated and measured quantities.

A different approach was proposed in [11], in which a suitable normalization forces the electromagnetic parameters of the PMSM to vary in a narrow range, rather independently of the motor size or shape. By applying a coherent normalization of the EKF algorithm, the covariance matrices $\mathbf{Q}$ and $\mathbf{R}$ generally fit for almost all standard PMSM drives. The technique facilitates the reuse of a tuned EKF on a different PMSM but, strictly speaking, it does not fix the problem of the first tuning, which remains on trial-and-error basis.

The Sage-Husa estimator, along with its variations, is widely used in adaptive EKF strategies, as in [12], where a modified Sage-Husa estimator is applied to a PMSM. Despite improvements in performance, Sage-Husa estimators require careful tuning, notably the selection of a forgetting factor b (ranging between 0 and 1) to define the amnestic factor d_k which weights the innovation and past noise values. The Sage-Husa adaptive Kalman filter and its variations achieve high estimation accuracy, but at the cost of increased computational complexity. Moreover, as previously mentioned, these algorithms require tuning factors.

Another pioneering alternative is the Ant Colony Optimization algorithm [13], which draws inspiration from the collective behavior of real ants, using volatile pheromone-based communication observed in biological ant colonies to tune the diagonal elements of the EKF covariance matrices. The four relevant parameters of $\mathbf{Q}$ and $\mathbf{R}$ are represented by six digits, each transformed into nodes that the ants traverse, establishing a return path to a virtual nest. Although the method is an intriguing attempt, the tuning process involves thousands of starts and stops in the speed loop, and its practical feasibility remains unproven.

The adaptive fading EKF described in [14], [15] employs an optimal adaptive fading factor $\lambda \geq 1$ to *blow up* the a-priori covariance estimation in case of increasing squared innovation, accelerating the estimation convergence by attempting to track this change. Even though the approach indirectly (if $\lambda > 1$) achieves the goal of enforcing a positive semi-definite covariance prediction, the filter may tend to be unstable. It furthermore requires manual tuning effort for both $\mathbf{Q}$ and $\mathbf{R}$. The innovation-based adaptive EKF reported in the same paper [15] is based on a steady-state approximation of the a-priori covariance, assuming that $\mathbf{Q}$ can be recovered from the last W samples of the innovation (W being the window length for the empirical covariance measurement). Obviously, the window size must be selected large enough such that it contains enough samples to accurately compute the empirical covariance, and small enough to remain responsive to changes in the process noise (avoiding the *dropping off* phenomenon [16]). If the contained information is insufficient, this direct approach can result in negative definite covariance estimates, potentially leading to observer divergence.

In the field of AC motor drives, significant contributions have recently been made using evolutionary algorithms, particularly for induction motors. Several studies propose updating the matrices $\mathbf{Q}$ and $\mathbf{R}$ based on motor operating conditions rather than using fixed values [18], [19]. However, evolutionary algorithms also require adjustment factors. They all share common drawbacks: high computational load, making them impractical when strong magnetic nonlinearity (as in the case of SynRM) demands very short control cycles, and a risk of suboptimal solutions that may not guarantee satisfactory performance.

Taking a step further, in [17] an extensive dataset obtained from a sensored drive was utilized to optimize the tuning of EKF matrices through a genetic algorithm. While the concept is intriguing, as it integrates early artificial intelligence principles into EKF tuning, it remains an offline method, with practical drawbacks such as the initial requirement for a sensored drive.

In [9], the authors highlight how, under changing operating conditions, the performance of the EKF deteriorates with fixed $\mathbf{Q}$ and $\mathbf{R}$ matrices. They propose a rather complex real-time procedure in which residual sequences are enforced to be orthogonal to each other, while simultaneously introducing a fading factor into the covariance matrix $\mathbf{Q}$ to adapt the Kalman gain matrix.

A more conventional alternative, which is notable for being effective and operational, is proposed in [20]. The paper first emphasizes the importance of the relationship between $\mathbf{Q}$ and $\mathbf{R}$ over their individual values in calculating the Kalman gain during the algorithm innovation step. Subsequently, an automatic tuning procedure for the EKF is outlined. Despite the

inclusion of experimental results, it is important to note that the study is confined to a PMSM with constant and perfectly known parameters.

Automating the tuning procedure is essential for expanding the application of the EKF in AC drives. To this goal, the paper at hand presents a primary–secondary(PS) structure [21] as a novel tuning paradigm and applies it to SynRM drives. The concept of the PS algorithm was initially introduced as an extension of the Unscented Kalman Filter (UKF) [22]. Subsequently, the same research group introduced a simplified version of the algorithm, using a linear Kalman Filter (KF) as a secondary filter, as in [23], [24], [25]. In [21], a work by the research group that introduced the *Primary Secondary* concept in the context of Kalman filters, the authors improve the manual tuning process significantly, obtaining an optimally designed adaptive filter. Actually, this good result comes from numerically solving an optimization problem, in which gathering several simulation data is the first offline step. Theoretically, even if matrices $\mathbf{Q}$ and $\mathbf{R}$ can be adapted simultaneously, the resulting filter would not be robust, since it is hard to distinguish between errors in both matrices. Thus, in [21] only the $\mathbf{R}$-matrix is updated based on that data, while the $\mathbf{Q}$-matrix is assumed to be known.

Both the adaptive fading EKF and the innovation-based adaptive EKF, as described in [15], along with our proposed PSKFapproach, incorporate some form of empirical feedback based on the past W samples of innovation and covariance. However, in the case of the PSKF, this feedback is treated as a stochastic variable rather than being deterministically trusted and directly used for the covariance update. This approach results in a more robust overall control system.

B. CONTRIBUTION AND STRUCTURE OF THE PAPER

This paper bridges the principle of PS structure, so far confined to aircraft engineering [22], [23], [24], [25], to a high-dynamic, highly nonlinear SynRM drive. It is worth to note that bridging theory to practice is not simply a matter of transposing algorithms; in many cases, the same theory, when applied to different systems, can yield significantly different outcomes. The application context is also crucial when choosing the most appropriate KF structure. In this work, we employ the Extended Kalman Filter (EKF), which we found to be particularly suitable for electric drive applications [26], over all the different KFs adopted in the cited references.

The PS structure proposed in this paper consists of a primaryEKF whose four-dimensional state vector is composed of the SynRM currents, speed, and position, and a innovation-based secondaryKF whose four-dimensional state vector consists of the elements of the covariance matrix $\mathbf{Q}_\mathrm{p}$ of the primaryEKF. In turn, the secondaryKF uses the innovation of the EKF to drive the convergence of its own state estimate.

The proposed PS approach enables the online determination and continuous tracking of the noise covariance matrix $\mathbf{Q}_\mathrm{p}$ in the EKF. A key advantage of this method is that the tuning effort is shifted from $\mathbf{Q}_\mathrm{p}$ to the covariance matrix $\mathbf{Q}_\mathrm{s}$ of the secondaryKF, which experiments demonstrated to be a far less critical task: As demonstrated by the experimental results presented in this paper, tuning $\mathbf{Q}_\mathrm{s}$ requires considerably less effort than direct tuning of $\mathbf{Q}_\mathrm{p}$. The primaryEKF and the secondaryKF operate simultaneously, with $\mathbf{Q}_\mathrm{p}$ being computed and updated online in accordance with the actual operating conditions of the drive. It is important to note that the proposed method does not significantly enhance estimation accuracy; rather, it achieves the same high-quality results that previously required tedious and time-consuming manual tuning of $\mathbf{Q}_\mathrm{p}$.

A distinction is also made between conventional experimental results and what are defined as real experimental results in this study. While other works typically either tune the EKF using real data or execute the EKF in parallel with a control system closed on measured variables, the present approach takes a further step by incorporating the estimated state variables of the EKF directly into the feedback loops of current and speed control in the motor control system. This real-time interaction between the EKF, the control system, and the actual motor within a live setup ensures a direct and practical validation of the proposed algorithm.

The paper is structured as follows. Section II recalls the mathematical model of the SynRM, while Section III provides the foundations of both the primaryEKF and secondaryKF algorithms. Section IV depicts the experimental setup and provides insight into the implementation of the proposed technique. This is followed by a detailed and comprehensive discussion of the tuning of the proposed PSKFand a performance comparison with a manually tuned EKF. Some conclusive remarks are drawn in Section V.

II. THE SYNRM MODEL EQUATIONS

For any given working point, the stator voltage balance equations of a SynRM can be expressed in a synchronous reference frame as

$$\mathbf{u}_\mathrm{dq} = R_s \mathbf{i}_\mathrm{dq} + \mathbf{L}_\mathrm{dq}^\mathrm{diff} \frac{\mathrm{d}\mathbf{i}_\mathrm{dq}}{\mathrm{dt}} + \omega_\mathrm{e} \mathbf{J} \boldsymbol{\lambda}_\mathrm{dq} \tag{1}$$

where $\mathbf{u}_\mathrm{dq} = [u_\mathrm{d}, u_\mathrm{q}]^\mathrm{T}$, $\mathbf{i}_\mathrm{dq} = [i_\mathrm{d}, i_\mathrm{q}]^\mathrm{T}$ are the SynRM stator voltages and current vectors, respectively. While R_s is the stator resistance, the *differential inductance* matrix and the operational matrix $\mathbf{J}$ are defined as

$$\mathbf{L}_\mathrm{dq}^\mathrm{diff} = \begin{bmatrix} \frac{\partial \lambda_d}{\partial i_d} & \frac{\partial \lambda_d}{\partial i_q} \\ \frac{\partial \lambda_q}{\partial i_d} & \frac{\partial \lambda_q}{\partial i_q} \end{bmatrix} \approx \begin{bmatrix} L_\mathrm{d}^\mathrm{diff} & 0 \\ 0 & L_\mathrm{q}^\mathrm{diff} \end{bmatrix}, \quad \mathbf{J} = \begin{bmatrix} 0 & -1 \\ 1 & 0 \end{bmatrix} \tag{2}$$

where $\mathbf{L}_\mathrm{dq}^\mathrm{diff}$ is calculated as the Jacobian of the flux linkages $\boldsymbol{\lambda}_\mathrm{dq}$ with respect to the currents $\mathbf{i}_\mathrm{dq}$.

The off-diagonal terms of $\mathbf{L}_\mathrm{dq}^\mathrm{diff}$ refer to cross-coupling effects. In principle, excluding information about cross-coupling could deteriorate the accuracy of the estimation. In [27] the Authors compute the error introduced by neglecting the mutual inductance, that applied to our case results in an angle estimation error of a few degrees. Unfortunately, this

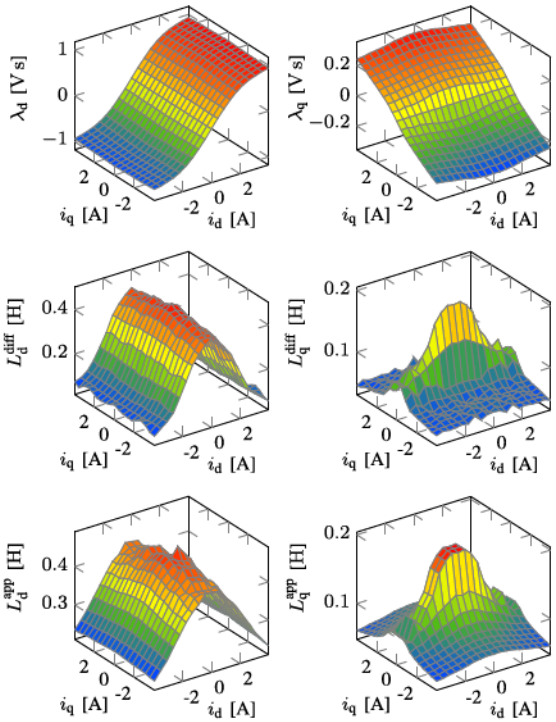

FIGURE 1. Flux linkages λ_{dq}, apparent inductances $\mathbf{L}_{dq}^{app}$, and differential inductances $\mathbf{L}_{dq}^{diff}$ of the SynRM used in the experiments (Table 1).

issue cannot be resolved simply by including mutual inductance in the model. In our case, the cross-coupling inductance is highly noisy, and both experimental and simulation results confirm that its inclusion increases estimation noise without providing any significant improvement. Therefore, although the data were available, they were not considered in this work. Anyway, for general purpose applications, especially if overload operation is required, the noise introduced by the adoption of L_{dq} can be reduced by smoothing the differential inductance tables to obtain more precise data and the mutual coupling can be included.

The stator flux linkage vector is $\boldsymbol{\lambda}_{dq} = [\lambda_d, \lambda_q]^T = \mathbf{L}_{dq}^{app}\mathbf{i}_{dq}$, where $\mathbf{L}_{dq}^{app} = \mathrm{diag}(L_d^{app}, L_q^{app})$ represents the so-called *apparent inductance* diagonal matrix. The elements of this matrix are simply the ratio of each flux linkage to the respective current. The electrical speed, denoted by ω_e, is equal to the pole pairs p times the rotor mechanical speed ω_m.

The magnetic model depicted in Fig. 1 has been derived through the elaboration of a series of measurements, as described in [28]. This model is crucial for the correct functioning of the observer, as detailed in Section IV. Nonetheless, while the model is important for the overall estimation performance, the consequences of limited position errors in inductance retrieval from the LUTs are negligible.

The literature does not provide a clear indication regarding the optimal reference frame for KF implementation. Model equations in a synchronous coordinate system are simpler. However, it should be noted that a coordinate transformation into the synchronous reference frame requires the electrical position of the SynRM, ϑ_e, which, in a sensorless drive, is one of the states to be estimated. Consequently, the EKF algorithm is developed in the stationary Clarke reference frame (α, β) as a more straightforward approach, as it includes the interdependence (coupling of the state variable's dynamics) of the currents with the angle within the Kalman filter algorithm, instead outside the algorithm.

To this aim, the model (1) is rewritten through the inverse Park transform as

$$\mathbf{u}_{\alpha\beta} = R_s \boldsymbol{i}_{\alpha\beta} + \mathbf{A}\frac{\mathrm{d}\boldsymbol{i}_{\alpha\beta}}{\mathrm{dt}} + \omega_e\,(\mathbf{B}+\mathbf{C})\,\boldsymbol{i}_{\alpha\beta} \tag{3}$$

Solving for the stator current dynamics, (3) yields

$$\frac{\mathrm{d}\mathbf{i}_{\alpha\beta}}{\mathrm{dt}} = \mathbf{A}^{-1}\left[\boldsymbol{u}_{\alpha\beta} - R_s\mathbf{i}_{\alpha\beta} - \omega_e\,(\mathbf{B}+\mathbf{C})\,\boldsymbol{i}_{\alpha\beta}\right] \tag{4}$$

where **A**, **B** and **C** are defined as

$$\mathbf{A} = \begin{bmatrix} L_\Sigma^{diff} + L_\Delta^{diff}\cos(2\vartheta_e) & L_\Delta^{diff}\sin(2\vartheta_e) \\ L_\Delta^{diff}\sin(2\vartheta_e) & L_\Sigma^{diff} - L_\Delta^{diff}\cos(2\vartheta_e) \end{bmatrix} \tag{5}$$

$$\mathbf{B} = \begin{bmatrix} -L_\Delta^{diff}\sin(2\vartheta_e) & L_\Sigma^{diff} + L_\Delta^{diff}\cos(2\vartheta_e) \\ -L_\Sigma^{diff} + L_\Delta^{diff}\cos(2\vartheta_e) & L_\Delta^{diff}\sin(2\vartheta_e) \end{bmatrix} \tag{6}$$

$$\mathbf{C} = \begin{bmatrix} -L_\Delta^{app}\sin(2\vartheta_e) & -L_\Sigma^{app} + L_\Delta^{app}\cos(2\vartheta_e) \\ L_\Sigma^{app} + L_\Delta^{app}\cos(2\vartheta_e) & L_\Delta^{app}\sin(2\vartheta_e) \end{bmatrix} \tag{7}$$

and $L_\Sigma^x = (L_d^x + L_q^x)/2$, $L_\Delta^x = (L_d^x - L_q^x)/2$, (^{x} = app, diff).

As for the mechanical model of the motor, an *infinite inertia* hypothesis is adopted, wherein the speed variation within the control cycle T_c is assumed to be negligible [29], [30]. This assumption leads to a mechanical model

$$\frac{\mathrm{d}\vartheta_e}{\mathrm{dt}} = \omega_e, \qquad \frac{\mathrm{d}\omega_e}{\mathrm{dt}} = 0. \tag{8}$$

III. PRIMARY–SECONDARYKALMAN FILTER

The flow chart of the proposed Primary-SecondaryKF algorithm is depicted in Fig. 2. In terms of notation, superscripts $\pm$ denote the quantity either *corrected* ($^+$) or *predicted* ($^-$) at the considered step. For example, $\hat{\mathbf{x}}^-(k)$ represents the predicted estimate of the state in step k. The subscripts p and s refer to the EKF and the secondaryKF, respectively.

The task of the primaryEKF is to provide the electrical position ϑ_e for the sensorless control of SynRM. The secondaryKF is responsible for supplying the diagonal elements of the $\mathbf{Q}_p$ matrix to the primaryEKF.

A. PRIMARYEKF

Assuming that the system behaves like an explicit discretization of the electrical (4) and mechanical (8) models, i.e.

$$\begin{aligned} \mathbf{x}_p(k) &= \mathbf{f}(\mathbf{x}_p(k-1), \mathbf{u}_p(k-1), \mathbf{w}_p(k-1)) \\ \mathbf{y}_p(k) &= \mathbf{h}(\mathbf{x}_p(k), \mathbf{u}(k), \mathbf{v}_p(k)) \end{aligned} \tag{9}$$

with states $\mathbf{x}_p = [i_\alpha,\ i_\beta,\ \omega_e,\ \vartheta_e]^T$, stator input voltages $\mathbf{u}_p = [u_\alpha,\ u_\beta]^T$, measured outputs $\mathbf{y}_p = [i_\alpha,\ i_\beta]^T$, process noise $\mathbf{w}_p$,

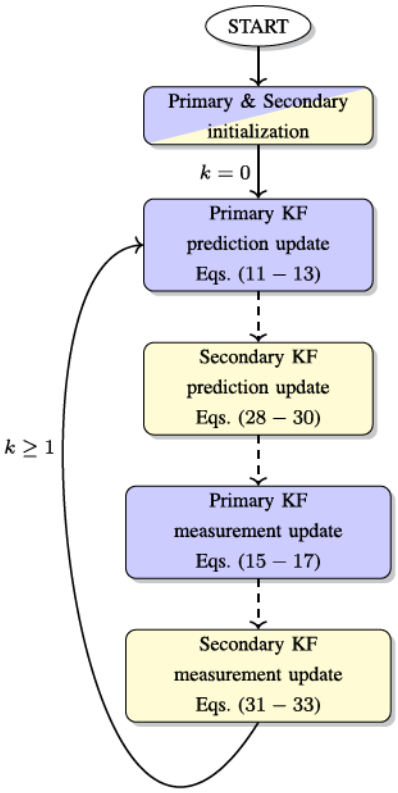

FIGURE 2. Flow chart of the proposed Primary–SecondaryKF algorithm.

measurement noise $\mathbf{v}_\mathrm{p}$, and considering the usual Kalman Filter assumptions of zero-mean Gaussian noise and uncertainty, and furthermore assuming that a sufficiently accurate model of the dynamics is available ($\hat{\mathbf{f}} \approx \mathbf{f}$), we can obtain the a-priori predictions for states and outputs of the primaryEKF as

$$\begin{aligned}\hat{\mathbf{x}}_\mathrm{p}^-(k) &= \hat{\mathbf{f}}(\hat{\mathbf{x}}_\mathrm{p}^+(k-1), \mathbf{u}_\mathrm{p}(k-1), \mathbf{0}) \\ \hat{\mathbf{y}}_\mathrm{p}(k) &= \hat{\mathbf{h}}(\hat{\mathbf{x}}_\mathrm{p}^-(k), \mathbf{u}_\mathrm{p}(k), \mathbf{0})\end{aligned} \tag{10}$$

Apart from the adapted matrix $\hat{\mathbf{Q}}_\mathrm{p}(k)$, the primaryEKF is a conventional EKF, described by the following steps:

- **Time Update**

$$\hat{\mathbf{x}}_\mathrm{p}^-(k) = \hat{\mathbf{f}}(\hat{\mathbf{x}}_\mathrm{p}^+(k-1), \mathbf{u}_\mathrm{p}(k-1), \mathbf{0}) \tag{11}$$

$$\hat{\mathbf{Q}}_\mathrm{p}(k) = \mathrm{diag}\left(\hat{\mathbf{x}}_\mathrm{s}^+(k-1)\right) \tag{12}$$

$$\mathbf{P}_\mathrm{p}^-(k) = \mathbf{J}_\mathrm{p}(k)\mathbf{P}_\mathrm{p}^+(k-1)\mathbf{J}_\mathrm{p}(k)^\mathrm{T} + \hat{\mathbf{Q}}_\mathrm{p}(k) \tag{13}$$

It should be noted that (12) is the noise covariance matrix of the EKF process, whose diagonal elements are the previous estimate of the secondaryKF. In (13), $\mathbf{J}_\mathrm{p}$ is the discrete-time state Jacobian matrix, evaluated in the last step's corrected estimates and defined as

$$\mathbf{J}_\mathrm{p}(k) = \frac{\partial \hat{\mathbf{x}}_\mathrm{p}^-(k)}{\partial \hat{\mathbf{x}}_\mathrm{p}^+(k-1)^\mathrm{T}}. \tag{14}$$

- **Measurement Update**

$$\mathbf{K}_\mathrm{p}(k) = \mathbf{P}_\mathrm{p}^-(k)\mathbf{H}_\mathrm{p}(k)^\mathrm{T}\left(\mathbf{H}_\mathrm{p}(k)\mathbf{P}_\mathrm{p}^-(k)\mathbf{H}_\mathrm{p}(k)^\mathrm{T} + \mathbf{R}_\mathrm{p}\right)^{-1} \tag{15}$$

$$\hat{\mathbf{x}}_\mathrm{p}^+(k) = \hat{\mathbf{x}}_\mathrm{p}^-(k) + \mathbf{K}_\mathrm{p}(k)\left(\mathbf{y}_\mathrm{p}(k) - \hat{\mathbf{y}}_\mathrm{p}(k)\right) \tag{16}$$

$$\mathbf{P}_\mathrm{p}^+(k) = \left(\mathbf{I}_{n\times n} - \mathbf{K}_\mathrm{p}(k)\mathbf{H}_\mathrm{p}(k)\right)\mathbf{P}_\mathrm{p}^-(k) \tag{17}$$

where $n = 4$ is the size of the state vector, $\hat{\mathbf{y}}_\mathrm{p}(k)$ are the predicted outputs, depending on $\hat{\mathbf{x}}_\mathrm{p}^-(k)$, $\mathbf{R}_\mathrm{p}$ relates to the variance of the measurement noise, and $\mathbf{H}_\mathrm{p}$ is the output Jacobian matrix, evaluated in the predicted estimates and defined as

$$\mathbf{H}_\mathrm{p}(k) = \frac{\partial \hat{\mathbf{y}}_\mathrm{p}(k)}{\partial \hat{\mathbf{x}}_\mathrm{p}^-(k)^\mathrm{T}}. \tag{18}$$

B. SECONDARYKF

Under the assumption that the process and measurement noise are Gaussian white, the matrices $\mathbf{Q}$ and $\mathbf{R}$ are diagonal [22], [31], therefore the estimation of the noise covariances means estimating the diagonal elements of the matrices. Given that measurement noise knowledge is given by the accuracy of current sensors, the focus is placed on process noise estimation. Therefore, the state vector of the secondaryfilter coincides with the diagonal elements of the $\mathbf{Q}$-matrix of the primary EKF, that is, $\mathbf{x}_\mathrm{s} = \mathrm{diag}\{\mathbf{Q}_\mathrm{p}\} = [q_{11,\mathrm{p}},\ q_{22,\mathrm{p}},\ q_{33,\mathrm{p}},\ q_{44,\mathrm{p}}]^\mathrm{T}$.

Because of uncertainty in the process noise dynamics, the discrete-time *prediction step* of the secondaryKF is given by

$$q_{ii,\mathrm{p}}(k) = q_{ii,\mathrm{p}}(k-1) \qquad i = 1, 2, 3, 4 \tag{19}$$

When it comes to the the secondarymeasurement update, the algorithm is based on processing the primaryinnovation $\boldsymbol{\nu}_p(k) = \mathbf{y}_\mathrm{p}(k) - \hat{\mathbf{y}}_\mathrm{p}(k)$ and its covariance $\mathbf{P}_\mathrm{p}^{\nu\nu}$, in particular the secondaryfilter aims to match the primaryerror covariance matrix $\mathbf{P}_\mathrm{p}^{\nu\nu}$ with empirical one $\hat{\mathbf{P}}_\mathrm{p}^{\nu\nu}$

$$\hat{\mathbf{P}}_\mathrm{p}^{\nu\nu} = \frac{1}{W}\sum_{j=k-W+1}^{k}\left(\boldsymbol{\nu}_\mathrm{p}(j) - \bar{\boldsymbol{\nu}}_\mathrm{p}(k)\right)\left(\boldsymbol{\nu}_\mathrm{p}(j) - \bar{\boldsymbol{\nu}}_\mathrm{p}(k)\right)^\mathrm{T} \tag{20}$$

where W is the window length, $\boldsymbol{\nu}_\mathrm{p}(j)$ is the innovation at time j, and $\bar{\boldsymbol{\nu}}_\mathrm{p}(k)$ is the average innovation over the whole window.

With these premises, the secondaryinnovation $\boldsymbol{\nu}_\mathrm{s}$ is defined as $\boldsymbol{\nu}_\mathrm{s} = \mathrm{diag}(\hat{\mathbf{P}}_\mathrm{p}^{\nu\nu}) - \mathrm{diag}(\mathbf{P}_\mathrm{p}^{\nu\nu})$. Therefore, the *measurement* (in the terminology of KF methods) supplied to the secondaryfilter consists of the diagonal elements of the empirical $\hat{\mathbf{P}}_\mathrm{p}^{\nu\nu}$, while the estimated output is the diagonal of the primaryfilter's internally-computed $\mathbf{P}_\mathrm{p}^{\nu\nu}$.

The secondaryKF output model is obtained by considering the standard KF error covariance matrix update equation [23]

$$\mathbf{P}_\mathrm{p}^+(k) = \mathbf{P}_\mathrm{p}^-(k) - \mathbf{K}_\mathrm{p}(k)\mathbf{P}_\mathrm{p}^{\nu\nu}(k)\mathbf{K}_\mathrm{p}^\mathrm{T}(k) \tag{21}$$

Now from (21) we can extract $\mathbf{P}_\mathrm{p}^{\nu\nu}(k)$ and consider just its diagonal elements

$$\mathrm{diag}\left\{\mathbf{P}_\mathrm{p}^{\nu\nu}(k)\right\} = \mathrm{diag}\left\{\mathbf{K}_\mathrm{p}^{\#}(k)(\mathbf{P}_\mathrm{p}^-(k) - \mathbf{P}_\mathrm{p}^+(k))\mathbf{K}_\mathrm{p}^{\#}(k)^\mathrm{T}\right\} \tag{22}$$

in which $\mathbf{K}_\mathrm{p}^{\#}$ represents the Moore-Penrose inverse of the primaryKalman gain $\mathbf{K}_\mathrm{p}$. The predicted outputs of the secondarysystem result as

$$\hat{\mathbf{y}}_\mathrm{s}(k) = \mathrm{diag}\left\{\mathbf{P}_\mathrm{p}^{\mathrm{yy}}(k)\right\} = \\ = \mathrm{diag}\left\{\mathbf{K}_\mathrm{p}^{\#}(k)(\mathbf{P}_\mathrm{p}^{-}(k) - \mathbf{P}_\mathrm{p}^{+}(k))\mathbf{K}_\mathrm{p}^{\#}(k)^{\mathrm{T}}\right\} \tag{23}$$

The matrix $\mathbf{P}_\mathrm{p}^{-}(k)$ can be expressed through (13) and inserted into the previous (23), to obtain

$$\begin{aligned}\hat{\mathbf{y}}_\mathrm{s}(k) &= \mathrm{diag}\left\{\mathbf{K}_\mathrm{p}^{\#}(k)\left(\mathbf{J}_\mathrm{p}(k)\mathbf{P}_\mathrm{p}^{+}(k-1)\mathbf{J}_\mathrm{p}(k)^{\mathrm{T}} + \hat{\mathbf{Q}}_\mathrm{p}(k)\right.\right. \\ &\quad \left.\left. -\mathbf{P}_\mathrm{p}^{+}(k)\right)\mathbf{K}_\mathrm{p}^{\#}(k)^{\mathrm{T}}\right\} \\ &= \mathrm{diag}\left\{\mathbf{K}_\mathrm{p}^{\#}(k)\hat{\mathbf{Q}}_\mathrm{p}(k)\mathbf{K}_\mathrm{p}^{\#}(k)^{\mathrm{T}}\right\} + \\ &\quad + \mathrm{diag}\left\{\mathbf{K}_\mathrm{p}^{\#}(k)\left(\mathbf{J}_\mathrm{p}(k)\mathbf{P}_\mathrm{p}^{+}(k-1)\mathbf{J}_\mathrm{p}(k)^{\mathrm{T}}\right.\right. \\ &\quad \left.\left. -\mathbf{P}_\mathrm{p}^{+}(k)\right)\mathbf{K}_\mathrm{p}^{\#}(k)^{\mathrm{T}}\right\} \\ &= \left(\mathbf{K}_\mathrm{p}^{\#}(k) \circ \mathbf{K}_\mathrm{p}^{\#}(k)\right)\mathrm{diag}\left\{\hat{\mathbf{Q}}_\mathrm{p}(k)\right\} + \\ &\quad + \mathrm{diag}\left\{\mathbf{K}_\mathrm{p}^{\#}(k)\left(\mathbf{J}_\mathrm{p}(k)\mathbf{P}_\mathrm{p}^{+}(k-1)\mathbf{J}_\mathrm{p}(k)^{\mathrm{T}}\right.\right. \\ &\quad \left.\left. -\mathbf{P}_\mathrm{p}^{+}(k)\right)\mathbf{K}_\mathrm{p}^{\#}(k)^{\mathrm{T}}\right\} \\ &= \mathbf{H}_\mathrm{s}(k)\hat{\mathbf{x}}_\mathrm{s}^{-}(k) + \mathbf{u}_\mathrm{s}(k)\end{aligned} \tag{24}$$

where the states $\hat{\mathbf{x}}_\mathrm{s}^{-}(k)$ and outputs $\hat{\mathbf{y}}_\mathrm{s}(k)$ together form the state space model for estimating the **Q**-matrix and $\mathbf{H}_\mathrm{s}(k)$ is the output Jacobian matrix. They are defined as follows:

$$\hat{\mathbf{x}}_\mathrm{s}^{-}(k) = \mathrm{diag}\left\{\hat{\mathbf{Q}}_\mathrm{p}(k)\right\} \tag{25}$$

$$\mathbf{H}_\mathrm{s}(k) = \mathbf{K}_\mathrm{p}^{\#}(k) \circ \mathbf{K}_\mathrm{p}^{\#}(k) \tag{26}$$

$$\mathbf{u}_\mathrm{s}(k) = \mathrm{diag}\left\{\mathbf{K}_\mathrm{p}^{\#}(k)\left(\mathbf{J}_\mathrm{p}(k)\mathbf{P}_\mathrm{p}^{+}(k-1)\mathbf{J}_\mathrm{p}(k)^{\mathrm{T}} - \mathbf{P}_\mathrm{p}^{+}(k)\right)\mathbf{K}_\mathrm{p}^{\#}(k)^{\mathrm{T}}\right\} \tag{27}$$

in which the symbol $\circ$ denotes element-wise multiplication.

After having considered the state and the output models, the secondaryKF structure is condensed in the following structure:

- **Time Update**

$$\hat{\mathbf{x}}_\mathrm{s}^{-}(k) = \hat{\mathbf{x}}_\mathrm{s}^{+}(k-1) \tag{28}$$

$$\mathbf{P}_\mathrm{s}^{-}(k) = \mathbf{P}_\mathrm{s}^{+}(k-1) + \mathbf{Q}_\mathrm{s}(k) \tag{29}$$

$$\hat{\mathbf{y}}_\mathrm{s}(k) = \mathbf{H}_\mathrm{s}(k)\hat{\mathbf{x}}_\mathrm{s}^{-}(k) + \mathbf{u}_\mathrm{s}(k) \tag{30}$$

  where $\mathbf{H}_\mathrm{s}(k)$ and $\mathbf{u}_\mathrm{s}(k)$ are defined in (26) and (27), respectively.

- **Measurement Update**

$$\mathbf{K}_\mathrm{s}(k) = \mathbf{P}_\mathrm{s}^{-}(k)\mathbf{H}_\mathrm{s}(k)^{\mathrm{T}}\left(\mathbf{H}_\mathrm{s}(k)\mathbf{P}_\mathrm{s}^{-}(k)\mathbf{H}_\mathrm{s}(k)^{\mathrm{T}} + \mathbf{R}_\mathrm{s}(k)\right)^{-1} \tag{31}$$

$$\hat{\mathbf{x}}_\mathrm{s}^{+}(k) = \hat{\mathbf{x}}_\mathrm{s}^{-}(k) + \mathbf{K}_\mathrm{s}(k)\left(\mathbf{y}_\mathrm{s}(k) - \hat{\mathbf{y}}_\mathrm{s}(k)\right) \tag{32}$$

$$\mathbf{P}_\mathrm{s}^{+}(k) = \left(\mathbf{I}_{n\times n} - \mathbf{K}_\mathrm{s}(k)\mathbf{H}_\mathrm{s}(k)\right)\mathbf{P}_\mathrm{s}^{-}(k) \tag{33}$$

where **I** is the identity matrix and $\mathbf{y}_\mathrm{s}$ corresponds to the diagonal of the *empirical* innovation covariance defined in (20), whereas $\hat{\mathbf{y}}_\mathrm{s}(k)$ is defined in (24).

C. FILTER CONVERGENCE CONDITIONS

With regards to the convergence of the proposed method, the following considerations are almost the same as the usually made for the standard EKF [15], since the primaryKF is a normal EKF with variable $\hat{\mathbf{Q}}_\mathrm{p}(k)$ and constant $\mathbf{R}_\mathrm{p}$, while the secondaryKF is a conventional linear KF with fixed noise covariances. For this reason, only the convergence of the primaryEKF will be discussed. The convergence of the primary is guaranteed if the following assumptions hold [32], [33]:

- Assumption 1
  1) The covariance matrices $\hat{\mathbf{Q}}_\mathrm{p}(k)$ and $\mathbf{R}_\mathrm{p}$ are bounded guaranteeing that $\hat{\mathbf{Q}}_\mathrm{p}(k)$ is always positive semi-definite, whereas $\mathbf{R}_\mathrm{p}$ is positive definite. There exist real numbers $q_\mathrm{p}^{\min}$, $q_\mathrm{p}^{\max}$, $r_\mathrm{p}^{\min}$ and $r_\mathrm{p}^{\max}$ such that

$$q_\mathrm{p}^{\min}\mathbf{I}_{4\times4} \le \hat{\mathbf{Q}}_\mathrm{p}(k) \le q_\mathrm{p}^{\max}\mathbf{I}_{4\times4} \tag{34}$$

$$r_\mathrm{p}^{\min}\mathbf{I}_{2\times2} \le \mathbf{R}_\mathrm{p} \le r_\mathrm{p}^{\max}\mathbf{I}_{2\times2} \tag{35}$$

     for each time step $k \ge 0$. This condition is satisfied since $\mathbf{R}_\mathrm{p}$ is fixed and its diagonal is composed of positive real numbers, whereas the diagonal of $\hat{\mathbf{Q}}_\mathrm{p}(k)$, whose elements are the secondaryKF estimates, is bounded in implementation between zero and positive real numbers.
  2) The matrices $\mathbf{J}_\mathrm{p}$ and $\mathbf{H}_\mathrm{p}$, equations (14) and (18) respectively, satisfy the uniform observability condition [29], [30].
  3) The initial covariance $\mathbf{P}_\mathrm{p}^{+}(0)$ is positive definite.
- Assumption 2
  1) There are positive real numbers $J_\mathrm{p}^{\max}$, $H_\mathrm{p}^{\max}$, $p_\mathrm{p}^{\min}$ and $p_\mathrm{p}^{\max}$ such that the following inequalities hold for each time step $k \ge 0$.

$$||\mathbf{J}_\mathrm{p}(k)|| \le J_\mathrm{p}^{\max} \tag{36}$$

$$||\mathbf{H}_\mathrm{p}(k)|| \le H_\mathrm{p}^{\max} \tag{37}$$

$$p_\mathrm{p}^{\min}\mathbf{I}_{4\times4} \le \mathbf{P}_\mathrm{p}(k) \le p_\mathrm{p}^{\max}\mathbf{I}_{4\times4} \tag{38}$$

  2) $\mathbf{J}_\mathrm{p}$, (14) is non-singular for each time $k \ge 0$.

IV. EXPERIMENTAL RESULTS

A. TEST BENCH AND CONTROL DESIGN

The experiments were carried out using a test bench comprising a SynRM, the nameplate data of which are detailed in Table 1, and a PMSM mechanically connected to the SynRM, serving as a virtual load. Both motors were fed by Space Voltage Modulation (SVM) inverters, sharing a 400 V DC-Link, with a switching frequency of 8 kHz. Drive control was

TABLE 1. System and SynRM Parameters

Parameters	Symbol	Unit	Value
Nominal torque	τ_n	N m	3.5
Nominal current	I_n	A	3
Nominal speed	ω_n	min^{-1}	1200
Stator resistance	R_s	Ω	4.72
unsat. d-axis inductance	L_d	mH	380
unsat. q-axis inductance	L_q	mH	85
pole pairs	p	\	2
Voltage Source Inverter, 2-levels IGBT			
DC voltage	u_{bus}	V	400
Dead-time	t_d	µs	2
Switching frequency	f_s	kHz	8
Control Platform		dSPACE MicroLabBox	
Control frequency	f_c	kHz	8

FIGURE 3. The experimental test bench.

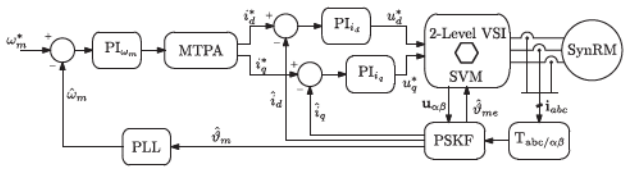

FIGURE 4. The proposed PSKF-based sensorless control of the SynRM.

implemented through a MicroLabBox dSpace Fast Control Prototype (FCP) system. The test bench is shown in Fig. 3.

The current control consists of two gain-scheduling PI controllers, whose implementation details are described in [34]. The PI gains were tuned to achieve a constant 150 Hz bandwidth with 70 deg phase margin. This eases the design of the outer speed control loop, which consists of a conventional PI controller, with antiwind-up and fixed bandwidth of 5 Hz. The current and speed control block diagram is reported in Fig. 4. All experiments were performed using the quantities estimated by the PSKFas feedback.

The speed is an estimated state variable and, in principle, could directly serve as speed feedback. However, the infinite inertia hypothesis in the motor model introduces dynamic estimation noise to the speed variable. While this noise does not compromise the accuracy of the EKF estimates, it is excessive for feedback control purposes, as it would lead to noise amplification in high-gain feedback scenarios. To mitigate this issue, a Phase-Locked Loop (PLL) filter is employed to recover the speed $\hat{\omega}_m$ from the estimated position $\hat{\vartheta}_p$. The PLL is tuned with a characteristic frequency of $\omega_0 = 2\pi \cdot 50\,\text{Hz}$ and a damping factor of D = 1. This filter provides smoother feedback and although it does not enhance dynamic performance, significantly improves speed tracking in steady-state conditions, as confirmed by experimental tests.

An approximate maximum torque per ampere (MTPA) strategy was implemented by dividing the output of the speed Proportional-Integral (PI$_{\omega_m}$) controller into equal current references, denoted i_d^* and i_q^*, which corresponds to setting the current vector phase θ_i^{MTPA} to 45 deg.

The magnetic model of SynRM, as utilized in the EKF model (4) and (5), is depicted in Fig. 1. Each lookup-table (LUT) consists of $19 \times 19 = 361$ values. Each value is a double precision variable, that requires 64 b = 8 B. Therefore the occupied memory is $361 \times 4 \times 8 = 11.28$ kB.

During the experiments, it has been found that the sensorless algorithm is improved by supplying the SynRM with a minimum d-axis current even with no load. A minimum d-axis current of $I_d^{\min} = I_n/3$ was established.

B. TUNING OF THE PROPOSED PSKF

The experiments involve a performance comparison between a manually tuned EKF and the proposed PSKF. In the first case, the trial-and-error approach yielded the values $\mathbf{Q}^{\text{EKF}} = \text{diag}(0.01, 0.01, 20, 0.001)$ and $\mathbf{R}^{\text{EKF}} = \text{diag}(0.001, 0.001)$, which remained constant thereafter. It should be noted that the measurement noise matrix $\mathbf{R}$ refers only to the noise introduced by the current sensors, since the output function $\mathbf{h}(\mathbf{x}_p(k), \mathbf{u}(k), \mathbf{v}_p(k))$ in (9) is linear.

Regarding the PSKF, the primaryfilter $\mathbf{Q}$ matrix was tuned and updated online by the secondaryKF, while the $\mathbf{R}$ matrix was obtained from the noise expected from the current sensors, following the same procedure as done for the EKF.

For the secondaryKF, the initial value of the state $\hat{\mathbf{x}}_s(0)$ was arbitrarily set to $\mathbf{x}_s(0) = [1, 1, 1, 1]^T$, and consequently $\hat{\mathbf{Q}}_p$ was initialized to the identity matrix. The covariance matrices were configured as $\mathbf{R}_s = r \cdot \text{diag}(1, 1)$ and $\mathbf{Q}_s = q \cdot \text{diag}(1, 1, 1, 1)$, respectively. The ratio q/r impacts the estimation performed by the secondaryKF and, in a cascade, influences the primaryEKF matrix $\hat{\mathbf{Q}}_p$. Our study found that a higher ratio leads to quicker (but noisier) convergence of the secondaryKF. In our simulations, a ratio value of $q/r = 100$ provided a satisfactory trade-off. The experiments confirmed this observation, but also highlighted that the value is not critical and can be varied quite broadly without negative consequences.

When dealing with unmodeled disturbances, such as dead times, highly nonlinear systems, or even when faced with substantial nonzero mean measurement noise, the predicted

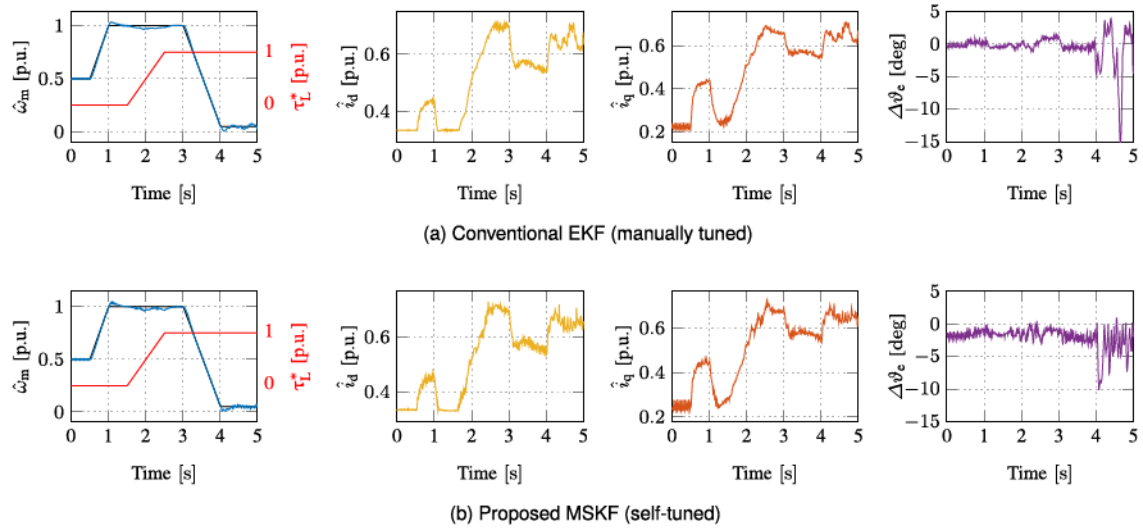

FIGURE 5. Minimum Speed at Rated Torque (MSRT) test for conventional EKF (upper row) and PSKF(lower row). From left to right: mechanical speed ω_m, currents on the d-axis i_d and the q-axis i_q, electrical position error $\Delta\vartheta_e$. All values refer to their respective nominal values as listed in Table 1.

change in covariance, $\mathbf{P}_p^- - \mathbf{P}_p^+$, may lose its positive definiteness. This is not allowable for a valid covariance matrix, as it would imply that it does not decrease in the correction step, leading to a potential divergence in the estimation process. To ensure a consistent estimation of the covariance matrix for the primaryEKF, we enforced the state estimate $\hat{\mathbf{x}}_s^-$ of the secondaryKF to always remain positive.

Preliminary simulation tests, later validated by experiments, revealed that the $\mathbf{Q}_p$ weight of the speed state variable, denoted as $q_{33,m}$, should have a lower bound greater than 0. Otherwise, in a steady state condition, the speed estimate ω_e enters an idle state where it becomes unresponsive to variations in speed reference or load torque, which is also called *dropping off* phenomenon [16]. As a result, the estimation error increases progressively until the secondaryKF adjusts the weight $q_{33,p}$. To avoid this situation, a minimum weight was established at $q_{33,p} \geq 5$ during the experimental phase. To summarize, we enforced a lower bound for the secondarystate as follows:

$$\mathbf{Q}_p \succeq \mathrm{diag}(0, 0, 5, 0) \tag{39}$$

One last aspect deserves attention: the length of the window W in (20) determines the number of innovation samples used by the secondaryfilter to update the primaryprocess noise weights.

In [15], a window length of 16 samples was selected as a trade-off between estimation performance and computational burden. The choice of window size heavily depends on the specific application, particularly the speed and load torque references to which it will be subjected. In the present case, with a speed loop bandwidth of 5 Hz and a maximum speed reference slope of 4800 rpm s^{-1}, a window of $W = 10$ was found to be the best choice. Selecting a small window size was necessary to manage the sharp and dynamic speed and load torque profiles used in the tests presented in Figs. 5 and 7. By adopting such window size, rapid and notable $q_{xx,p}$ variations are likely to occur. Further reducing the window size is not advisable, since it increases the risk of unstable filter behavior. On the other hand, using larger window sizes, such as $W = 128$ as suggested by [15], makes the PSKFless sensitive to disturbances but hampers its ability to adapt to process noise variances during transients.

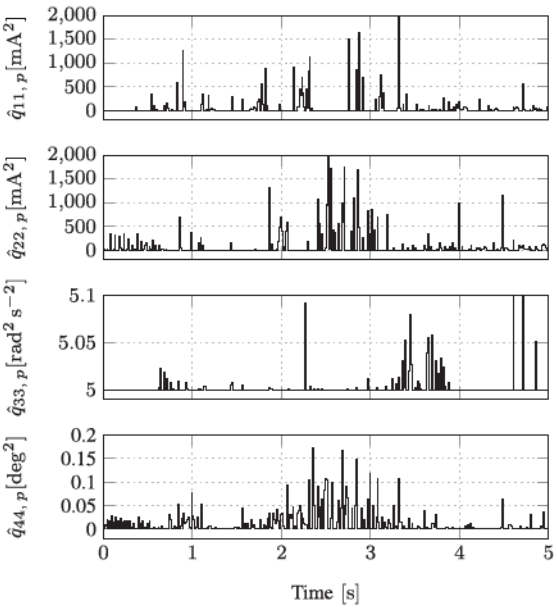

FIGURE 6. Diagonal elements of $\hat{Q}_p$ in the MSRT test, depicted in Fig. 5.

C. PERFORMANCE COMPARISON

A comprehensive measurement campaign was conducted with the objective of comparing the manually tuned EKF with the proposed PSKFtopology, which incorporates self-adapted online tuning. The results of the experiments presented in this section are summarized in Table 2. Throughout each test (detailed in the following subsections), the quantities

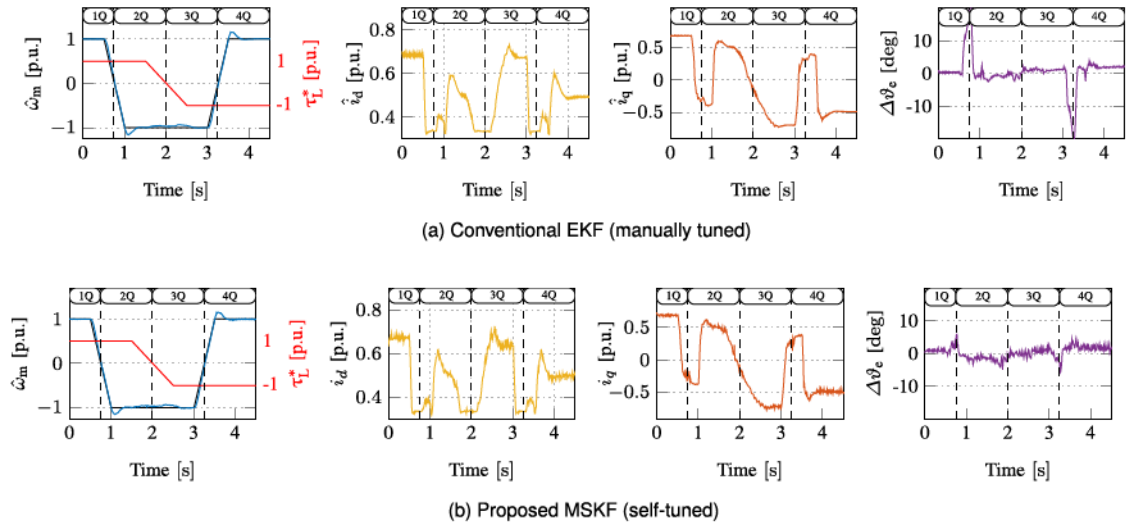

FIGURE 7. Four-Quadrant Operation (FQO) test for conventional EKF (upper row) and PSKF(lower row). From left to right: mechanical speed ω_m, currents on the d-axis i_d and the q-axis i_q, electrical position error $\Delta\vartheta_e$. All values refer to their respective nominal values as listed in Table 1.

TABLE 2. Mean Squared Error (MSE)

Variable	Symbol	Unit	Test	EKF	PSKF	Fig.
Mechanical speed	ω_m	rpm^2	MSRT	38.6	100.7	5
			FQO	160.5	172.2	7
			SSS	268.7	65.9	9
d-axis current	i_d	mA^2	MSRT	4783	2583	5
			FQO	4471	2754	7
			SSS	3799	3058	\
q-axis current	i_q	mA^2	MSRT	6652	2447	5
			FQO	9208	3108	7
			SSS	14680	21955	\
Electrical position	ϑ_e	deg^2	MSRT	4.63	2.37	5
			FQO	22.38	4.62	7
			SSS	35.24	57.56	9

estimated by the EKF and, after coordinate transformation, by the PSKF, namely $\hat{\mathbf{x}} = [\omega_m,\ i_d,\ i_q,\ \vartheta_e]$, were collected at the control frequency (Table 1), along with the measured values (note that the measurements were available in the prototype only for comparison purposes). For each state variable $\hat{x}$ of the state vector $\hat{\mathbf{x}}$, the Mean Squared Error (MSE) was computed as follows:

$$\mathrm{MSE}_x = \frac{1}{N}\sum_{i=1}^{N}\left(\hat{x}_i - x_i^{\mathrm{meas}}\right)^2 \tag{40}$$

where N is the total number of collected states during the test.

1) THE MINIMUM SPEED AT RATED TORQUE (MSRT) TEST

The test starts by setting a positive speed reference at no load. Before initiating the transient load torque at $t = 0.5$ s, the SynRM accelerates from 0.5 p.u. to 1 p.u., still under no load conditions. Subsequently, the load torque is increased to its nominal value, after which the reference speed is reduced to 5% of the rated speed. This minimum threshold was determined through repeated tests until uncontrollable oscillations occurred at low speed. In many application fields, such as electrical pumps, a 1:20 full-load speed range is acceptable. It is worth noting that the inability to operate below a certain minimum speed is a common drawback of all EKF-based observers, regardless of how well-tuned they may be. The condition for observability at zero speed has been derived, for the linear magnetic model case, in [30] and [29]. In both cases, the observability at zero speed is guaranteed if the derivatives of the currents are different than zero, highlighting the need for either simple open-loop I-f techniques or some kind of high-frequency current injection [35], [36].

The results are presented in Fig. 5. In the leftmost figure, the black line represents the speed reference provided to the SynRM, while the red line depicts the torque reference applied to the PMSM, which serves as a virtual load. The blue trace corresponds to the estimated speed, denoted as $\hat{\omega}_m$ and obtained from the PLL block in Fig. 4.

Continuing from left to right, the other figures show the estimated current on the d-axis $\hat{i}_d$, the estimated current on the q-axis $\hat{i}_q$ and the electrical position error $\Delta\vartheta_e = \hat{\vartheta}_e - \vartheta_e^{\mathrm{meas}}$ during the speed and torque transients.

At full load and stable minimum speed, both the EKF and the PSKFexhibit oscillations in the position estimate. The position error remains limited to between $[0 - 3\,^\circ]$ for the proposed PSKFand between $[0 - 5\,^\circ]$ for the conventional EKF. However, both filters remain indefinitely convergent, even after the time period shown in Fig. 5(a).

The estimated diagonal elements of $\hat{\boldsymbol{Q}}_p$ are depicted in Fig. 6. The diagonal elements of $\hat{\boldsymbol{Q}}_p$ are updated online by the secondaryKF, which adapts the primaryfilter to the varying conditions of the SynRM.

Referring to Table 2, it is evident that the MSE speed is lower in the EKF than in the PSKF. However, PSKFprovides

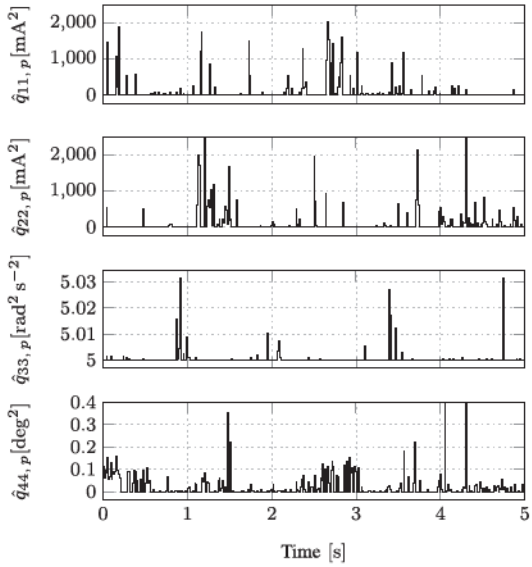

FIGURE 8. Diagonal elements of $\hat{Q}_p$ in the FQO test, depicted in Fig. 7.

more accurate results for both currents and the electrical position.

2) THE FOUR-QUADRANT OPERATION (FQO) TEST

The test begins with a positive nominal speed reference and a rated load torque, τ_L^*. While maintaining the same torque, a speed reversal is initiated at $t = 0.5$ s, transitioning from the first quadrant (labeled as 1Q) to the second quadrant (2Q), as shown in Fig. 7. At $t = 1.5$ s, a load torque reversal is triggered, moving from 1, p.u. to -1, p.u.. Finally, at $t = 3$ s, a second speed reversal is imposed to exit the third quadrant (3Q) and enter the fourth quadrant (4Q).

It should be noted that the electrical position estimation error tends to increase during speed zero crossings, a well-known limitation in sensorless techniques that do not utilize injected signals for estimation [29], [30]. However, when comparing Fig. 7(a) and (b), it becomes evident that the PSKFexhibits a lower $\Delta\vartheta_e$ than the EKF.

The manually tuned EKF provides a slightly better speed MSE compared to the PSKF, with a difference of only 12 rpm^2. Again, the PSKFoutperforms the EKF in the other state variables (the MSE is half for i_d), one third for i_q and just one fifth for ϑ_e). The estimated diagonal elements of $\hat{Q}_p$ are depicted in Fig. 8.

The slight improvements shown in Fig. 5 and in Fig. 7 can be attributed to the adaptive nature of the proposed tuning procedure, which accommodates varying environmental conditions.

3) THE STEP STARTING FROM STANDSTILL (SSS) TEST

The test evaluates the drive performance when the motor starts from a complete standstill and a sudden change in speed reference is applied. In particular, at t = 0.5, a speed step is executed up to half the nominal speed. The state of the proposed PSKFis initialized randomly.

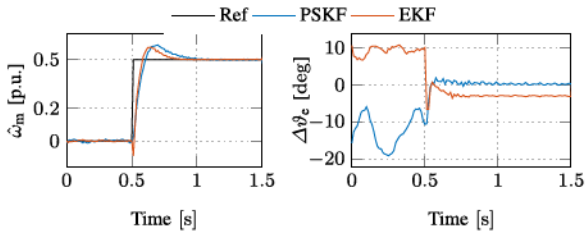

FIGURE 9. Step Starting from Standstill (SSS) test: mechanical speed (left) and electrical position error (right). All values are referenced to their respective nominal values as listed in Table 1.

The test shows that both EKF and PSKFare capable of initiating motion from a standstill condition. In terms of speed, as shown in Fig. 9, they exhibit nearly identical responses. Note that the EKF is already tuned, while the PSKFrelies just on the self-tuning at standstill and no load.

Regarding the electrical position error $\Delta\vartheta_e$ displayed in Fig. 9, prior to the step command, the EKF position ϑ_e appears stable, with an error of approximately 10 deg. In contrast, the position error derived from the PSKFappears less stable, oscillating between -7 deg and -20 deg. However, following the speed step, the position error for the EKF stabilizes around -3 deg, while the PSKFsolution settles approximately at 0.4 deg.

In contrast to previous tests, the EKF exhibits an MSE higher than that of the PSKFfor the speed variable, while it performs better than that of the PSKFwhen considering $\mathbf{i}_{dq}$ and ϑ_e. To understand this behavior, it is important to note that the MSE calculations are performed over the entire test time. As shown in Fig. 9, before the initiation of the speed step, $\Delta\vartheta_e^{\text{PSKF}}$ is greater than in the case of the EKF, and this behavior significantly influences the MSE calculation. Between t = 1.2 and t = 1.5, the MSE related to electrical position drops to 8.92 deg^2 for the EKF and to 0.27 deg^2 for the PSKF.

4) SENSITIVITY TO PARAMETER MISMATCH

The measurement noise is associated with the sensors used for current measurements, which are assumed to be known. The adaptation proposed in the paper focuses solely on the $\mathbf{Q}_p$ matrix, that is, on the stochastic properties of process noise. The effect of process noise variation was investigated by modifying the parameters, namely resistance and flux linkage mismatches. The resistance mismatch is attributed to temperature variations, which result in an increase in the actual stator resistance compared to the value used in the model (4). Six experiments are carried out under steady-state conditions, with a speed reference of 0.1, p.u. and rated load torque, each with a progressively increasing resistance mismatch, by modifying the resistance value in the model used by the observer, and not by physically changing the motor. The results, including the mean electrical position error and MSE, are presented in Table 3. The resistance mismatch is expressed as the ratio R_s^{KF}/R_s, where R_s^{KF} explicitly represents the value used in

TABLE 3. Resistance Mismatch Test

R_s^{KF}/R_s	Mean ($\Delta\vartheta_e$)		Unit	MSE (ϑ_e)		Unit
	EKF	PSKF		EKF	PSKF	
1	−1.24	−2.45		3.68	7.72	
0.9	1.2	−2.69		4.8	9.17	
0.8	4.41	−2.98	deg	20.59	11.73	deg^2
0.7	6.22	−2.68		39.65	13.06	
0.6	8.21	−3.64		68.46	17.69	
0.5	9.85	−3.72		98.97	20.16	

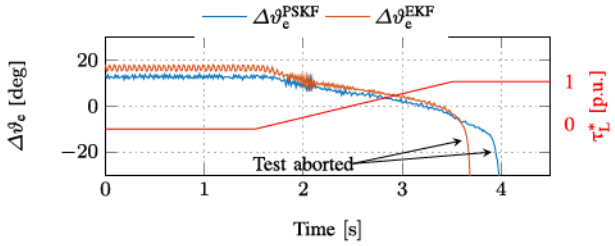

FIGURE 10. Electrical position error, performance in case of constant inductance model (conventional EKF vs. proposed PSKF).

the filter model, while R_s corresponds to the nominal value documented in Table 1.

When the resistance mismatch is within the range of $R_s^{KF} = 0.9R_s$, the EKF provides more accurate results. However, as the mismatch increases, the PSKFoffers a more precise estimation in terms of position error. It should be noted that the mean of $\Delta\vartheta_e$ is deeply affected by the resistor value used in the filter. However, the mean value of the PSKFcase remains almost constant throughout the range of resistance values, resulting in less dependence on the estimation of the resistance mismatch. The mean value shown in Table 3 was calculated by averaging the electrical position error over 1600 samples.

A second set of experiments was conducted to evaluate the robustness against potential discrepancies in the magnetic model used in the Kalman filter equations (5). The test involved replacing the magnetic maps shown in Fig. 1 with constant unsaturated inductance values listed in Table1 (referred to as *linear model*). The speed was maintained at a constant value of 0.5 p.u., while a ramp up of the load torque to the full load torque was applied, as illustrated in Fig. 10. Before the onset of the load torque, the electrical position error was approximately 17 deg for the EKF and 13 deg for the PSKF, with less oscillation. Both the EKF and the PSKFproved unable to cope with the substantial magnetic mismatch at full load due to motor saturation. The PSKFexhibited a delayed decline, which offered limited improvement. However, setting the load torque ramp to 95% of the full load, both filters passed the test.

5) EXECUTION TIME

As one would expect, the computational load of the PSKFis heavier than that of the conventional EKF, as it involves two simultaneously operating Kalman Filters. In the experiments, we used an integrated test bench for fast prototyping, which primarily consists of a dSpace control board and a PC-based Matlab-Simulink environment. Once the system is programmed in this environment, a real-time interface compiles the code and uploads it to the dSpace board. The compilation utilizes linear algebra libraries designed for real-time embedded systems, exploiting properties like sparsity to accelerate matrix computations. Additionally, floating-point acceleration units help offload tasks from the processor.

TABLE 4. Execution Times of the Control Algorithm Elements

Routine	Magnetic Model	Execution Time
Control cycle	\	125 µs
Speed & Current Control	\	22 µs
Conventional EKF	Linear	14.7 µs
	Nonlinear	15.6 µs
Proposed PSKF	Linear	16.6 µs
	Nonlinear	17.5 µs

Table 4 reports the execution time. It is worth to note that the secondaryKF adds only 1.9 µs to the execution time with respect to the EKF, which in percentage corresponds to just a 12% increment. This amount of time seems reasonable considering the low complexity of the secondaryKF. It consists of a linear KF, and the time update (28) is absent. The remaining time is due to the computation of the Kalman gain and the empirical innovation covariance matrix (20).

Considering that there are already examples of working industrial products including EKF implementations, an additional 12% of calculations will not pose a difficult challenge in actual microcontroller-based implementations of possible final products powered by PSKF. Available low-cost microcontrollers will be able to handle the optimized code in any case, since it is possible to offload parallelizable code like the secondaryKF structure or control algorithm calculations to secondary processor cores.

It is worth noting that the use of magnetic maps in Fig. 1 through Look-Up Tables (LUTs) requires an additional 0.9 µs due to memory access and subsequent value interpolation.

V. CONCLUSION

The proposed PSKFalgorithm eliminates the conventional trial-and-error manual tuning of the covariance matrix $\mathbf{Q}_p$ of the EKF. The responsibility for tuning the primaryEKF is delegated to the secondaryKF, which in turn is easily and efficiently tuned through the ratio q/r. Performance comparisons between manually tuned EKF and PSKFdemonstrate that streamlining the tuning process does not compromise the quality of the estimate. The 12% increase in processing time is considered reasonable in exchange for avoiding the laborious manual tuning of the primaryEKF. By eliminating the tedious and complex trial-and-error tuning process, the proposed algorithm represents a significant step toward more autonomous electrical drives.

APPENDIX A DISCRETE-TIME STATE JACOBIAN MATRIX

By considering the time update function $\hat{\mathbf{f}}$ in (14) and deriving it with respect to the state vector $\hat{\mathbf{x}}_\mathrm{p}^+(k-1)$, we obtain the state Jacobian matrix

$$\boldsymbol{J}_\mathrm{p}(k) = \left.\frac{\partial \hat{\mathbf{f}}(\hat{\mathbf{x}}_\mathrm{p}^+(k-1), \mathbf{u}_\mathrm{p}(k-1))}{\partial \hat{\mathbf{x}}_\mathrm{p}^+(k-1)^T}\right|_{\hat{\mathbf{x}}_\mathrm{p}^+(k-1),\, \boldsymbol{u}_\mathrm{m}(k-1)} = \begin{bmatrix} J_{11} & J_{12} & J_{13} & J_{14} \\ J_{21} & J_{22} & J_{23} & J_{24} \\ J_{31} & J_{32} & J_{33} & J_{34} \\ J_{41} & J_{42} & J_{43} & J_{44} \end{bmatrix} \tag{41}$$

where the elements J_{ij} (for $i, j = 1, \ldots, n$) are grouped into matrices for the sake of brevity. For instance, the matrix $\boldsymbol{J}_{m-n,r-s}$ is composed as follows:

$$\boldsymbol{J}_{m-n,r-s} = \begin{bmatrix} J_{m1} & \ldots & J_{mr} \\ \vdots & \ldots & \vdots \\ J_{n1} & \ldots & J_{ns} \end{bmatrix} \tag{42}$$

where $m-n$ indicates the indexes from m to n and similarly for $r-s$. The sub-matrices of $\boldsymbol{J}_\mathrm{m}$, in which T_s is the sampling time, are:

$$\begin{aligned} \boldsymbol{J}_{1-2,1-2} &= \boldsymbol{I}_{2\times 2} \\ &\quad - T_s\, \boldsymbol{A}^{-1}(k)\,[R_s + \omega_e(k)\,(\boldsymbol{B}(k) + \boldsymbol{C}(k))] \\ \boldsymbol{J}_{1-2,3} &= -T_s\, \boldsymbol{A}^{-1}(k)\,(\boldsymbol{B}(k) + \boldsymbol{C}(k))\, i_{\alpha\beta}(k) \\ \boldsymbol{J}_{1-2,4} &= T_s\, \frac{\partial \boldsymbol{A}^{-1}(k)}{\partial \vartheta_e(k)}\,[u_{\alpha\beta}(k) - R_s\, i_{\alpha\beta}(k) \\ &\quad - \omega_e(k)\,(\boldsymbol{B}(k) + \boldsymbol{C}(k))\, i_{\alpha\beta}(k)] \\ &\quad - T_s\, \boldsymbol{A}^{-1}(k)\omega_e(k)\left(\frac{\partial \boldsymbol{B}(k)}{\partial \vartheta_e(k)} + \frac{\partial \boldsymbol{C}(k)}{\partial \vartheta_e(k)}\right) i_{\alpha\beta}(k) \\ \boldsymbol{J}_{3-4,1-4} &= \begin{bmatrix} 0 & 0 & 1 & 0 \\ 0 & 0 & T_s & 1 \end{bmatrix} \end{aligned} \tag{43}$$

in which

$$\boldsymbol{A}^{-1}(k) = \frac{1}{L_\mathrm{d}^\mathrm{diff} L_\mathrm{q}^\mathrm{diff}} \begin{bmatrix} L_\Sigma^\mathrm{diff} - L_\Delta^\mathrm{diff} \cos(2\vartheta_\mathrm{e}(k)) & -L_\Delta^\mathrm{diff} \sin(2\vartheta_\mathrm{e}(k)) \\ -L_\Delta^\mathrm{diff} \sin(2\vartheta_\mathrm{e}(k)) & L_\Sigma^\mathrm{diff} + L_\Delta^\mathrm{diff} \cos(2\vartheta_\mathrm{e}(k)) \end{bmatrix} \tag{44}$$

and the derivatives result as

$$\begin{aligned} \frac{\partial \boldsymbol{A}^{-1}(k)}{\partial \vartheta_e(k)} &= \frac{2L_\Delta^\mathrm{diff}}{L_\mathrm{d}^\mathrm{diff} L_\mathrm{q}^\mathrm{diff}} \begin{bmatrix} \sin(2\vartheta_e(k)) & -\cos(2\vartheta_e(k)) \\ -\cos(2\vartheta_e(k)) & -\sin(2\vartheta_e(k)) \end{bmatrix} \\ \frac{\partial \boldsymbol{B}(k)}{\partial \vartheta_e(k)} &= 2L_\Delta^\mathrm{diff} \begin{bmatrix} -\cos(2\vartheta_e(k)) & -\sin(2\vartheta_e(k)) \\ -\sin(2\vartheta_e(k)) & \cos(2\vartheta_e(k)) \end{bmatrix} \\ \frac{\partial \boldsymbol{C}(k)}{\partial \vartheta_e(k)} &= 2L_\Delta^\mathrm{app} \begin{bmatrix} -\cos(2\vartheta_e(k)) & -\sin(2\vartheta_e(k)) \\ -\sin(2\vartheta_e(k)) & \cos(2\vartheta_e(k)) \end{bmatrix} \end{aligned} \tag{45}$$

REFERENCES

[1] A. Varatharajan, P. Pescetto, and G. Pellegrino, "Injectionless sensorless control of synchronous reluctance machine for zero to low speeds region," in *Proc. IEEE 9th Int. Symp. Sensorless Control Elect. Drives*, 2018, pp. 72–77, doi: 10.1109/SLED.2018.8486061.

[2] S. Julier and J. Uhlmann, "Unscented filtering and nonlinear estimation," *Proc. IEEE*, vol. 92, no. 3, pp. 401–422, Mar. 2004, doi: 10.1109/JPROC.2003.823141.

[3] D. Simon, *Optimal State Estimation*. Hoboken, NJ, USA: Wiley, Jan. 2006, doi: 10.1002/0470045345.

[4] F. Gao, Z. Yin, P. Zhang, Y. Zhang, and Y. Zhang, "A position sensorless control method robust to inductance mismatch for SynRM based on generalized multiple model resonant Kalman filter," *IEEE Trans. Power Electron.*, vol. 39, no. 5, pp. 5510–5521, May 2024, doi: 10.1109/TPEL.2024.3368334.

[5] F. Gao, Z. Yin, C. Bai, D. Yuan, and J. Liu, "A lag compensation-enhanced adaptive quasi-fading Kalman filter for sensorless control of synchronous reluctance motor," *IEEE Trans. Power Electron.*, vol. 37, no. 12, pp. 15322–15337, Dec. 2022, doi: 10.1109/TPEL.2022.3194519.

[6] F. Gao, Z. Yin, C. Bai, D. Yuan, and J. Liu, "Speed sensorless control method of synchronous reluctance motor based on resonant Kalman filter," *IEEE Trans. Ind. Electron.*, vol. 70, no. 8, pp. 7627–7641, Aug. 2023, doi: 10.1109/TIE.2022.3213920.

[7] P. Mercorelli, "A two-stage augmented extended Kalman filter as an observer for sensorless valve control in Camless internal combustion engines," *IEEE Trans. Ind. Electron.*, vol. 59, no. 11, pp. 4236–4247, Nov. 2012, doi: 10.1109/TIE.2012.2192892.

[8] P. Mercorelli, "A hysteresis hybrid extended Kalman filter as an observer for sensorless valve control in camless internal combustion engines," *IEEE Trans. Ind. Appl.*, vol. 48, no. 6, pp. 1940–1949, Nov./Dec. 2012, doi: 10.1109/TIA.2012.2226193.

[9] Z. Yin, G. Li, Y. Zhang, and J. Liu, "Symmetric-strong-tracking-extended-Kalman-filter-based sensorless control of induction motor drives for modeling error reduction," *IEEE Trans. Ind. Informat.*, vol. 15, no. 2, pp. 650–662, Feb. 2019, doi: 10.1109/TII.2018.2810850.

[10] K. Myers and B. Tapley, "Adaptive sequential estimation with unknown noise statistics," *IEEE Trans. Autom. Control*, vol. 21, no. 4, pp. 520–523, Aug. 1976.

[11] S. Bolognani, L. Tubiana, and M. Zigliotto, "Extended Kalman filter tuning in sensorless PMSM drives," *IEEE Trans. Ind. Appl.*, vol. 39, no. 6, pp. 1741–1747, Nov./Dec. 2003, doi: 10.1109/TIA.2003.818991.

[12] X. Wang, A. Wang, D. Wang, Y. Xiong, B. Liang, and Y. Qi, "A modified sage-Husa adaptive Kalman filter for state estimation of electric vehicle servo control system," *Energy Rep.*, vol. 8, pp. 20–27, Aug. 2022, doi: 10.1016/j.egyr.2022.02.105. [Online]. Available: http://dx.doi.org/10.1016/j.egyr.2022.02.105

[13] A. Wang, Q. Wang, C. Hu, Z. Qian, L. Ju, and J. Liu, "An EFK for PMSM sensorless control based on noise model identification using ant colony algorithm," in *Proc. 2009 Int. Conf. Elect. Mach. Syst.*, 2009, pp. 1–4.

[14] E. Zerdali, R. Yildiz, R. Inan, R. Demir, and M. Barut, "Adaptive fading extended Kalman filter based speed-sensorless induction motor drive," in *Proc. 2018 XIII Int. Conf. Elect. Mach.*, Sep. 2018, pp. 1367–1373, doi: 10.1109/icelmach.2018.8507168. [Online]. Available: http://dx.doi.org/10.1109/ICELMACH.2018.8507168

[15] E. Zerdali, "A comparative study on adaptive EKF observers for state and parameter estimation of induction motor," *IEEE Trans. Energy Convers.*, vol. 35, no. 3, pp. 1443–1452, Sep. 2020, doi: 10.1109/TEC.2020.2979850.

[16] S. Liu, "An adaptive Kalman filter for dynamic estimation of harmonic signals," in *Proc. 8th Int. Conf. Harmon. Qual. Power Proc. (Cat. No.98EX227)*, 1998, vol. 2, pp. 636–640, doi: 10.1109/ICHQP.1998.760120.

[17] K. Shi, T. Chan, Y. Wong, and S. Ho, "Speed estimation of an induction motor drive using an optimized extended Kalman filter," *IEEE Trans. Ind. Electron.*, vol. 49, no. 1, pp. 124–133, Feb. 2002, doi: 10.1109/41.982256.

[18] M. L. Jayaramu, H. N. Suresh, M. S. Bhaskar, D. Almakhles, S. Padmanaban, and U. Subramaniam, "Real-time implementation of extended Kalman filter observer with improved speed estimation for sensorless control," *IEEE Access*, vol. 9, pp. 50452–50465, 2021, doi: 10.1109/access.2021.3069676. [Online]. Available: http://dx.doi.org/10.1109/ACCESS.2021.3069676

[19] E. Zerdali and M. Barut, "The comparisons of optimized extended Kalman filters for speed-sensorless control of induction motors," *IEEE Trans. Ind. Electron.*, vol. 64, no. 6, pp. 4340–4351, Jun. 2017, doi: 10.1109/TIE.2017.2674579.

[20] L. Ortombina, D. Pasqualotto, F. Tinazzi, and M. Zigliotto, "Automatic tuning procedure at standstill for extended Kalman filter in sensorless control of permanent magnet synchronous motors," in *Proc. IEEE 10th Int. Symp. Sensorless Control Elect. Drives*, 2019, pp. 1–6, doi: 10.1109/SLED.2019.8896350.

[21] B. Ritter, E. Mora, A. Schild, B. Doekemeijer, and U. Konigorski, "Adaptive master-slave cubature Kalman filters subject to state inequality constraints for wind turbine state estimation," in *Proc. 2019 Amer. Control Conf.*, 2019, pp. 3482–3487, doi: 10.23919/ACC.2019.8814411.

[22] Q. Song and Y. He, "Adaptive unscented Kalman filter for estimation of modelling errors for helicopter," in *Proc. 2009 IEEE Int. Conf. Robot. Biomimetics*, 2009, pp. 2463–2467, doi: 10.1109/ROBIO.2009.5420406.

[23] S. Ritter, "Nonlinear state estimation and noise adaptive Kalman filter design for wind turbines," PhD thesis, Technische Universität Darmstadt, 2020.

[24] Q. Juntong, H. Jianda, and W. Zhenwei, "Rotorcraft UAV actuator failure estimation with KF-based adaptive UKF algorithm," in *Proc. 2008 Amer. Control Conf.*, 2008, pp. 1618–1623, doi: 10.1109/ACC.2008.4586723.

[25] M. Mohamed and I. Kar, "Aerodynamic parameter estimation using adaptive unscented Kalman filter," *Aircr. Eng. Aerosp. Technol.: An Int. J.*, vol. 85, pp. 267–279, 2013, doi: 10.1108/AEAT-Mar-2011-0038.

[26] S. Rigon, B. Haus, P. Mercorelli, and M. Zigliotto, "Comparison between UKF and EKF in sensorless synchronous reluctance motor drives," *IEEE Open J. Power Electron.*, vol. 5, pp. 1562–1572, 2024, doi: 10.1109/OJPEL.2024.3469533.

[27] C. Li, G. Wang, G. Zhang, D. Xu, and D. Xiao, "Saliency-based sensorless control for SYNRM drives with suppression of position estimation error," *IEEE Trans. Ind. Electron.*, vol. 66, no. 8, pp. 5839–5849, Aug. 2019, doi: 10.1109/TIE.2018.2874585.

[28] E. Armando, R. I. Bojoi, P. Guglielmi, G. Pellegrino, and M. Pastorelli, "Experimental identification of the magnetic model of synchronous machines," *IEEE Trans. Ind. Appl.*, vol. 49, no. 5, pp. 2116–2125, Sep./Oct. 2013, doi: 10.1109/TIA.2013.2258876.

[29] P. Vaclavek, P. Blaha, and I. Herman, "AC drive observability analysis," *IEEE Trans. Ind. Electron.*, vol. 60, no. 8, pp. 3047–3059, Aug. 2013, doi: 10.1109/TIE.2012.2203775.

[30] R. Caro, C. A. Silva, R. Pérez, and J. I. Yuz, "Sensorless control of a SynRM for the whole speed range based on a nonlinear observability analysis," in *Proc. 2017 IEEE Int. Conf. Ind. Technol.*, Mar. 2017, pp. 336–341, doi: 10.1109/ICIT.2017.7913253.

[31] Q. Song, Z. Jiang, and J. Han, "Noise covariance identification based adaptive UKF with application to mobile robot systems," in *Proc. 2007 IEEE Int. Conf. Robot. Autom.*, Apr. 2007, pp. 4164–4169, doi: 10.1109/robot.2007.364119.

[32] K. Reif, S. Gunther, E. Yaz, and R. Unbehauen, "Stochastic stability of the discrete-time extended Kalman filter," *IEEE Trans. Autom. Control*, vol. 44, no. 4, pp. 714–728, Apr. 1999, doi: 10.1109/9.754809.

[33] F. Alonge, T. Cangemi, F. D'Ippolito, A. Fagiolini, and A. Sferlazza, "Convergence analysis of extended Kalman filter for sensorless control of induction motor," *IEEE Trans. Ind. Electron.*, vol. 62, no. 4, pp. 2341–2352, Apr. 2015, doi: 10.1109/TIE.2014.2355133.

[34] R. Antonello, L. Ortombina, F. Tinazzi, and M. Zigliotto, "Advanced current control of synchronous reluctance motors," in *Proc. IEEE 12th Int. Conf. Power Electron. Drive Syst.*, 2017, pp. 1,037–1,042, doi: 10.1109/PEDS.2017.8289150.

[35] M. Pacha and S. Zossak, "Improved simple I-F open-loop start-up of PMSM drives without speed or position sensor," in *Proc. 2019 IEEE 10th Int. Symp. Sensorless Control Elect. Drives*, Sep. 2019, pp. 1–6, doi: 10.1109/SLED.2019.8896231.

[36] M. Berto, L. Alberti, V. Manzolini, and S. Bolognani, "Computation of self-sensing capabilities of synchronous machines for rotating high frequency voltage injection sensorless control," *IEEE Trans. Ind. Electron.*, vol. 69, no. 4, pp. 3324–3333, Apr. 2022, doi: 10.1109/TIE.2021.3071710.

SAVERIO RIGON (Member, IEEE) was born in Vicenza, Italy, in 1996. He received the B.S. and M.S. degrees in mechatronic engineering from the University of Padua, Vicenza, Italy, in 2018 and 2021, respectively. He is currently working toward the Ph.D. degree in mechatronics with the Department of Management and Engineering. His research interests include sensorless control of ac motor drives and Kalman filters applications.

BENEDIKT HAUS received the M.Sc. (Hons.) degree in automation and control from the Clausthal University of Technology, Clausthal-Zellerfeld, Germany, in 2016, and the Ph.D. degree in applied control engineering from the Leuphana University, Lüneburg, Germany, in 2020. His research interests include control applications and observer design, especially Kalman filters in practical applications, with an emphasis on interdisciplinary applications from nonengineering fields.

PAOLO MERCORELLI (Member, IEEE) received the master's degree in electronic engineering from the University of Florence, Florence, Italy, in 1992, and the Ph.D. degree in systems engineering from the University of Bologna, Bologna, Italy, in 1998. From 2005 to 2011, he was an Associate Professor of process informatics with the Ostfalia University of Applied Sciences, Wolfsburg, Germany. Since 2012, he has been a Full Professor of control and drive systems with Leuphana University of Lueneburg, Lueneburg, Germany. His current research interests include mechatronics, automatic control, and signal processing.

MAURO ZIGLIOTTO (Senior Member, IEEE) received a degree in electronic engineering from the University of Padova, Padua, Italy, in 1988. Until 1992, he worked in industry as the R&D Manager and then in Udine as an Associate Professor, leading the Electric Drives Laboratory. Since 2008, he has been a Full Professor of electrical machines and drives with the University of Padova. His research interests include innovative control and modeling, self-commissioning and sensorless ac drives, and the application of AI techniques under the *smarter ac drives* paradigm.